Topological characters in Fe($Te_{1-x}Se_x$) thin films

Xianxin Wu,[1] Shengshan Qin,[1] Yi Liang,[1] Heng Fan,[1,2] and Jiangping Hu[1,2,3,*]
[1]*Institute of Physics, Chinese Academy of Sciences, Beijing 100190, China*
[2]*Collaborative Innovation Center of Quantum Matter, Beijing 100190, China*
[3]*Department of Physics, Purdue University, West Lafayette, Indiana 47907, USA*
(Received 8 July 2015; revised manuscript received 15 December 2015; published 17 March 2016)

We investigate topological properties in the Fe(Te,Se) thin films. We find that the single layer $FeTe_{1-x}Se_x$ has nontrivial Z_2 topological invariance which originates from the parity exchange at the Γ point of the Brillouin zone. The nontrivial topology is mainly controlled by the Te(Se) height. Adjusting the anion height, which can be realized as the function of lattice constants and x in $FeTe_{1-x}Se_x$, can drive a topological phase transition. In a bulk material, the two-dimensional Z_2 topology invariance is extended to a strong three-dimensional one. In a thin film, we predict that the topological invariance oscillates with the number of layers. The results can also be applied to iron pnictides. Our research establishes $FeTe_{1-x}Se_x$ as a unique system to integrate high-T_c superconductivity and topological properties in a single electronic structure.

DOI: 10.1103/PhysRevB.93.115129

I. INTRODUCTION

Recently, topological insulators (TIs) [1–3] and iron-based superconductors [4,5] have attracted enormous attention in condensed matter physics. Most topological insulators are semiconductors with strong spin-orbit coupling in which the bulk gap protects surface or edge states depending on dimensionality. Their band structures are attributed to p orbitals. Iron-based superconductors, including iron pnictides and iron chalcogenides, are multiorbital electronic systems in which the electronic structures are mainly attributed to Fe $3d$ orbitals. Therefore, these two systems appear to be distantly apart. However, the combination of topological insulators and superconductors is known to generate novel physics, for example, Majorana fermions [6,7]. The usual way to integrate TIs and superconductivity is through superconducting proximity effect by making TI-superconductor heterostructures. Iron-based superconductors, due to their short coherent length and material incompatibility, are not suitable to such an integration.

However, recently, pioneer studies suggest that iron-based superconductors can carry intrinsic nontrivial topological properties. Two examples have been provided. One is the single layer FeSe grown on $SrTiO_3$ substrate where nontrivial Z_2 topology can be tuned through the band inversion at the M point in the Brillouin zone [8]. The other is $CaFeAs_2$ where nontrivial topology exists on additional As layers that are inserted between FeAs layers [9,10]. Although these results are encouraging, in the first case, a fine-tuning is required and in the second case, the topological properties are not from the layers that are responsible for high temperature superconductivity.

In this paper, we report that a single layer $FeTe_{1-x}Se_x$ with x less than a critical value x_c which is estimated to around 0.7, carries nontrivial Z_2 topological invariance that originated from the parity exchange at the Γ point. We identify that the nontrivial topology is mainly controlled by the Te(Se) height. Adjusting the anion height, which can be realized as the function of lattice constants and x in $FeTe_{1-x}Se_x$, can drive a topological phase transition. An effective model is constructed to explicitly describe the topological physics. In a thin film, it exhibits oscillation behavior with a trilayer structure being topologically trivial. The results can also be applied to iron pnictides. These results establish $FeTe_{1-x}Se_x$ as a unique system to integrate high-T_c superconductivity and topological properties in a single electronic structure.

II. Z_2 TOPOLOGICAL INVARIANCE IN THE BAND STRUCTURE OF A SINGLE LAYER FeTe

The crystal structure of FeTe (FeSe) is shown in Fig. 1. In order to gain insight into the nontrivial topological properties, first we analyze a topologically trivial case, the band structure of monolayer FeTe with lattice constant $a = 3.925$ Å, where the lattice constant is close to that of monolayer FeSe on $SrTiO_3$ [11–13]. In Fig. 2(a), the band structure of monolayer FeTe is plotted. Comparing the bands with spin-orbit coupling (SOC) (red lines) and without SOC (gray lines), we find that SOC has two main effects: (1) the twofold degenerate E_g bands at Γ are split into E_{g+} and E_{g-}; (2) the Dirac cone in the Γ-M line is also gapped. The latter makes a local gap at every k point in the Brillouin zone, which is important for defining the topological invariant discussed in the following. The parities of the eigenstates at Γ near the Fermi level are shown in Fig. 2(a). The odd parity state A_{2u} is contributed by Fe d_{xy} orbitals strongly coupled with Te p_z orbitals. The two even parity states E_{g+} and E_{g-} are attributed to Fe d_{xz}, d_{yz} strongly hybridized with Te p_x, p_y orbitals, while the other even parity state is mainly attributed to d_{xy} orbitals. Even though SOC is relatively weak in iron, the separation between E_{g+} and E_{g-} is large because the E_g states involve both Fe $3d$ and Te $5p$ states. With SOC, each band at X and M is fourfold degenerate and contains two Kramers pairs, which are protected by the crystal symmetry. The two Kramers pairs at M are related to each other by the mirror reflection on the XZ plane $\hat{g}_1 = \{\sigma^X|00\}$ but the two Kramers pairs at X are governed by the mirror reflection on the YZ plane $\hat{g}_2 = \{\sigma^Y|00\}$ [14]. As the inversion operator $\hat{I} = \{i|\frac{1}{2}\frac{1}{2}\}$ anticommutates with $\hat{g}_1$ at M and $\hat{g}_2$ at X, the two Kramers pairs at M and X have opposite parities. The

*jphu@iphy.ac.cn

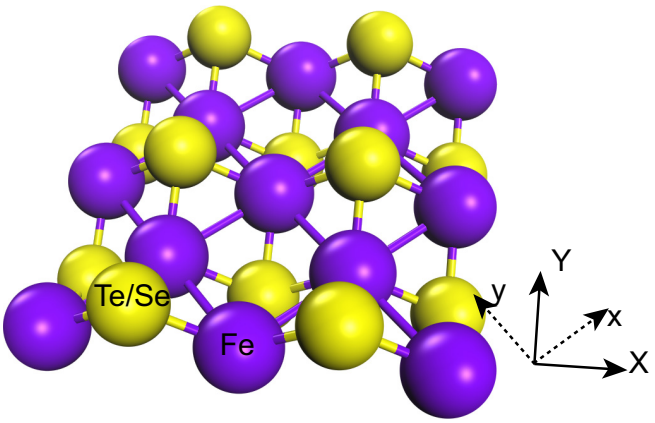

FIG. 1. Schematic view of the structure of anti-PbO-type monolayer FeTe(FeSe). The space group is $P4/nmm$. The $X(Y)$ is along Fe-Te/Se direction and $x(y)$ is along Fe-Fe direction.

band structure in Fig. 2(a) is topologically trivial according to the calculation of parity product of occupied states at the four time-reversal-invariant momenta [15].

III. ANION HEIGHT AND TOPOLOGICAL PHASE TRANSITION

One can notice that the two states A_{2u} and E_{g+} at Γ, which have opposite parities, are separated by a small gap about 0.09 eV. If the gap can be closed and reopened, the inversion between the two states will drive the system into a Z_2 topologically nontrivial phase because of the change of the overall parity character.

We find that this inversion takes place in the monolayer FeTe with a fully relaxed lattice constant parameter $a = 3.805$ Å. In Fig. 2(b), we plot the band structure of monolayer FeTe, where the two states A_{2u} and E_{g+} at Γ are clearly inverted. We further investigate the origin of this band inversion and find that it is controlled by the Te height and lattice constants. We define Δ_s and Δ_n as the energy differences between A_{2u} and E_{g+} states with SOC and without SOC, respectively. The Te height d, Δ_s, and Δ_n as functions of lattice constants are shown in Fig. 3(a). As the lattice constant decreases, the anion height increases

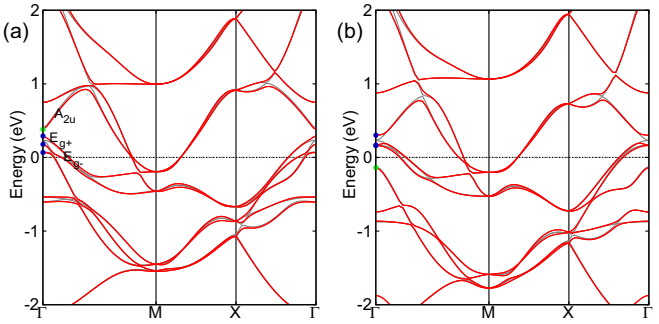

FIG. 2. Band structures for monolayer FeTe. (a) $a = 3.925$ Å and (b) $a = 3.805$ Å. The red solid lines represent the band with SOC and the gray lines the band without SOC. The parities of the eigenstates at Γ near the Fermi level are shown: blue circles for even parities and green circles for odd parities.

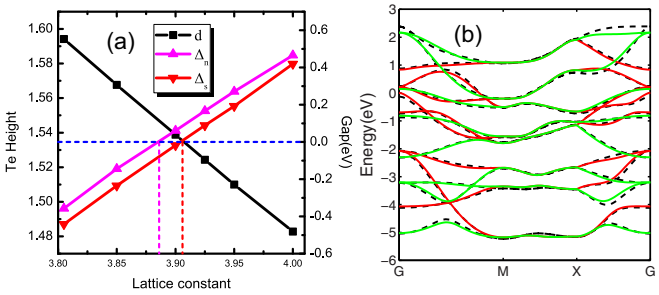

FIG. 3. Gaps and anion height as functions of lattice constant and tight binding band structure. (a) The Te height d and the gaps Δ_n and Δ_s as functions of the in-plane lattice constant. Both Te height and lattice constant are given in angstrom. (b) Band structures of monolayer FeTe without SOC from tight binding model and DFT. The red lines represent "k" bands and the green lines represent "$k + Q$" bands. The black dashed lines represent the DFT bands.

and the A_{2u} state sinks while the E_{g+} state rises, resulting in a decrease of Δ_s and Δ_n. Our calculations with SOC show that the phase transition occurs at $a = 3.905$ Å, where the corresponding Te height is $d = 1.535$ Å. For $a < 3.905$ Å, the system becomes topologically nontrivial. When $3.886 < a < 3.905$, Δ_s is negative but Δ_n is positive, indicating that the band inversion is completely driven by SOC, similar to that in Bi_2Se_3 [16]. Δ_n is negative for $a < 3.886$ Å and band inversion has happened without SOC, leaving the two E_g bands quadratic touching, which is the case shown in Fig. 3(b).

As the anions height can also be tuned by the concentration of Se in $FeTe_{1-x}Se_x$, the topological phase transition can take place by changing the Se concentration. To estimate the critical concentration, x_c, we take the experimental data of the lattice constants. The Se heights in FeSe and $FeTe_{0.5}Se_{0.5}$ are 1.46 Å and 1.589 Å [17,18], respectively. The topological phase transition point is roughly at $x_c = 0.7$ by assuming that the anion height is linear with respect to the Se concentration in $FeTe_{1-x}Se_x$ [19].

IV. TIGHT BINDING MODEL AND EFFECTIVE MODEL

To understand the parity exchange at Γ, we start from a tight binding model of the FeTe system. A general model including Fe d and X (X = Te,Se) p oribtals for iron-based superconductors can be written as

$$H_t = \sum_{\alpha\beta}\sum_{mn}\sum_{ij}\left(t^{mn}_{\alpha\beta,ij} + \epsilon_m\delta_{mn}\delta_{\alpha\beta}\delta_{ij}\right)c^{\dagger}_{\alpha m\sigma}(i)c_{\beta n\sigma}(j). \quad (1)$$

Here, α and β label the sublattices (A and B for Fe and Te). σ labels the spin and m and n label the d and p orbitals. i and j label lattice sites. $t^{mn}_{\alpha\beta,ij}$ are the corresponding hopping parameters. ϵ_m are the on-site energies of d or p orbitals. $c^{\dagger}_{\alpha m\sigma}(i)$ creates a spin-σ electron in the m orbital of the α sublattice at site i. As detailed in Appendix C, we can eliminate the sublattice index by writing the Hamiltonian in momentum space with respect to one Fe unit cell,

$$H_t = \sum_{\sigma,k\in BZ1}\phi^{\dagger}_{\sigma}(k)A(k)\phi_{\sigma}(k). \quad (2)$$

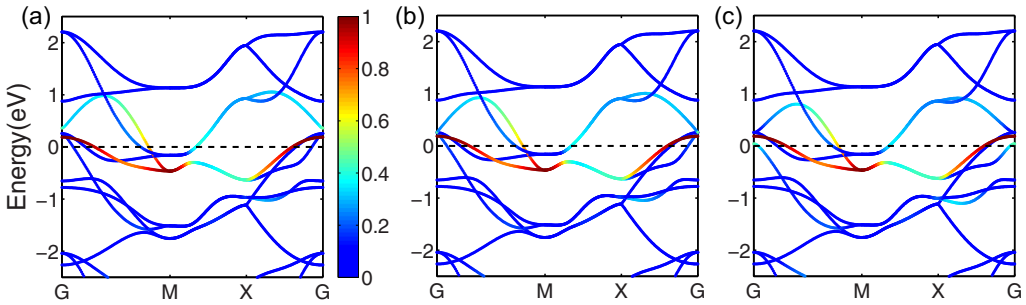

FIG. 4. The band structures with different hopping parameters q_{xy}^{43}. (a) $q_{xy}^{43} = 0.649$ eV. (b) $q_{xy}^{43} = 0.624$ eV. (c) $q_{xy}^{43} = 0.569$ eV. The color represents the weights of Fe d_{xy} orbitals. The A_{2u} state at Γ point sinks with the decreasing of q_{xy}^{43}.

In this case, as the inversion symmetry exchange the two sublattices, at Γ and M points the parity of $c_m(0)$ is even and $c_m(Q)$ odd for α being d-orbital while the parity of $c_m(0)$ is odd and $c_m(Q)$ even for α being p orbital with $Q = (\pi,\pi)$ [20,21].

Without SOC, the H_t can be constructed, as shown in Fig. 3(b), by fitting the density functional theory (DFT) band structure and the corresponding hopping parameters are given in appendix Table II. The red bands are referred to as "k" bands and the green ones are referred to as "$k + Q$" bands. We find that the band inversion is mainly controlled by the coupling between the Fe d orbital and the Te p orbital, which is described by the hopping parameter q_{xy}^{43}, the nearest neighbor (NN) hopping between Fe d_{xy} and Te p_z. As the lattice constant increases, the height of Te in monolayer FeTe decreases and the coupling between the Fe d orbital and the Te p orbital becomes stronger so that q_{xy}^{43} changes significantly. In Figs. 4(a)–4(c), we plot the band structures with different q_{xy}^{43}. As the q_{xy}^{43} decreases, the odd parity A_{2u} band sinks below the even parity bands.

How to understand this effect of q_{xy}^{43}? From the tight binding Hamiltonian, we know that the NN coupling term between Fe d_{xy} and Te p_z is $4q_{xy}^{43}\cos(k_x/2)\cos(k_y/2)$. Thus, at the Γ point this coupling vanishes in the "$k + Q$" bands. However, it is maximized at Γ in the "k" bands. The energy difference between the two coupled states is proportional to the coupling parameter. Therefore, the top state at Γ sinks with the decrease of q_{xy}^{43}. When the gap between the A_{2u} and E_g states is less than 80 meV, SOC can induce band inversion. When the A_{2u} state sinks below the E_g state, away from the Γ point the d_{xy} orbital can couple with the d_{xz} and d_{yz} orbitals, which produces an anticrossing. After the parity exchange, shown in Fig. 4(c), the system becomes topologically nontrivial with SOC.

An effective Hamiltonian can be derived to capture the parity exchange bands near the Γ point by including SOC. The detailed construction is provided in Appendix D. Focusing on the Γ point, the d_{xz} and d_{yz} orbitals couple with the p_x and p_y orbitals and the d_{xy} orbital couples with the p_z orbital. We combine them to form new bases and in the basis $\Psi_{\text{eff}}(k) = [c_{1+,\uparrow}(k), c_{-1+,\uparrow}(k), c_{0+,\uparrow}(k), c_{-1+,\downarrow}(k), c_{1+,\downarrow}(k), c_{0+,\downarrow}(k)]^T$, we can get the effective model around the Γ point as

$$H_{\text{eff}} = \sum_k \Psi_{\text{eff}}^{\dagger}(k) h_{\text{eff}}(k) \Psi_{\text{eff}}(k), \tag{3}$$

$$h_{\text{eff}}(k) = \begin{pmatrix} h_1(k) & 0 \\ 0 & h_1^{\star}(-k) \end{pmatrix}. \tag{4}$$

The $h_1(k)$ is a 3×3 matrix given in Appendix D. The bands of this effective model can capture the DFT bands around the Γ point (see Fig. 8 in appendix). As the band energy attributed to the $c_{-1+,\uparrow}(k)$ is typically much lower, the six-band structure can be further approximated by a minimum effective four-band structure in the new basis $\tilde{\Psi}_{\text{eff}}(k) = [c_{1+,\uparrow}(k), c_{0+,\uparrow}(k), c_{-1+,\downarrow}(k), c_{0+,\downarrow}(k)]^T$; the final

TABLE I. Parameters in the four-band effective model for monolayer FeTe with different lattice constants.

Lattice (Å)	C (eV)	M (eV)	D(eV Å^2)	B (eV Å^2)	A (eV Å)
3.805	0.082	−0.221	3.381	−4.122	2.318
3.9	0.284	−0.009	−0.880	−1.157	1.287
3.925	0.336	0.045	−0.586	−0.100	1.426

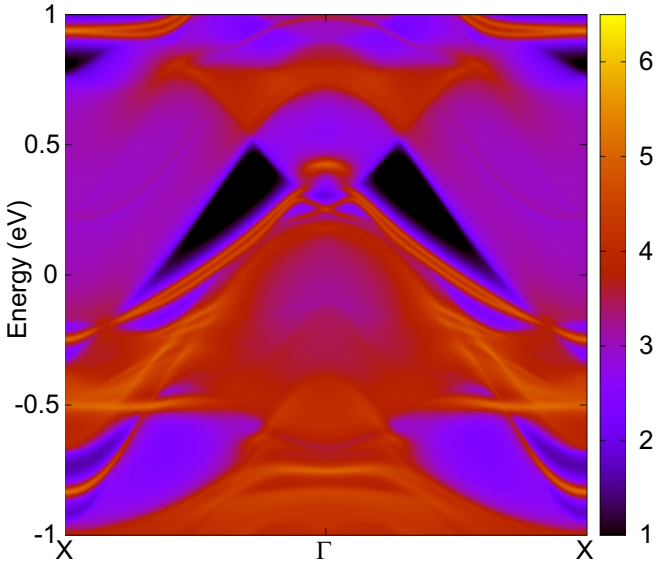

FIG. 5. Energy and momentum dependence of the LDOS for the monolayer FeTe with $a = 3.805$ Å on the [100] edge. The higher LDOS is represented by brighter color. The ingap edge states can be clearly seen around the Γ point, which clearly indicates the nontrivial topology of monolayer FeTe.

effective Hamiltonian reads

$$H_{\text{eff}} = \sum_k \tilde{\Psi}^{\dagger}_{\text{eff}}(k)\tilde{h}_{\text{eff}}(k)\tilde{\Psi}_{\text{eff}}(k), \tag{5}$$

$$\tilde{h}_{\text{eff}}(k) = \epsilon_0(k) + \begin{pmatrix} -M(k) & Ak_+ & 0 & 0 \\ Ak_- & M(k) & 0 & 0 \\ 0 & 0 & -M(k) & -Ak_- \\ 0 & 0 & -Ak_+ & M(k) \end{pmatrix}, \tag{6}$$

where $\epsilon_0(k) = C - D(k_x^2 + k_y^2)$, $M(k) = M - B(k_x^2 + k_y^2)$, and $k_\pm = k_x \pm ik_y$. $M > 0$ corresponds to the normal regime, whereas $M < 0$ corresponds to the inverted regime, namely, the topologically nontrivial regime. The fitting parameters for different lattice constants are given in Table I. The bands of this model are given in Fig. 8 in Appendix D.

As discussed above, the monolayer FeTe is in the topologically nontrivial region. To show the effect of nontrivial topology, we calculate the surface Green's function of the semi-infinite system using an iterative method [22,23]. The edge local density of states (LDOS) of (100) edge for FeTe monolayer is shown in Fig. 5. The nontrivial edge states confirm the conclusion that monolayer FeTe is topologically nontrivial by parity analysis.

V. MULTI-FeTe LAYERS

The band structures of a bilayer and trilayer FeTe are given in Figs. 8 and 9 in the Appendix. We find that the bilayer and quad-layer systems are topologically nontrivial while the trilayer system is topologically trivial. This oscillation behavior is similar to that of Bi_2Se_3 thin films [24] and can be argued as follows (detailed in Appendix E). We can assume that there are only couplings in A_{2u} states between two nearest-neighbor layers. In a bilayer system, a bonding and an antibonding band are formed due to the coupling between two layers. If the coupling is strong enough, the antibonding band gains energy and becomes unoccupied. Therefore, the overall topological Z_2 character is the same as in the single layer. In a trilayer system, it is only one band among the three reconstructed bands that due to the layer coupling becomes unoccupied. In this case, the overall Z_2 character changes and becomes trivial. In a quad-layer system, there are two bands among the four reconstructed bands which gain energy. However, one of them gains a much smaller energy. If this energy gain is not large enough to lift the band unoccupied, the system has the nontrivial Z_2 topological invariance. The argument can be quantified as detailed in Appendix E. Let Δ be the energy required to make the A_{2u} band unoccupied at the Γ point and J is the layer coupling strength. To be consistent with our finding, we must have $0.62 < \frac{\Delta}{J} < 1$. According to our calculation, $\frac{\Delta}{J}$ is about 0.9, confirming the validity of our arguments.

VI. DISCUSSION

According to the aforementioned discussion, we know that the height of Te(Se) or lattice constants play an essential role in the topological phase transition. Besides tuning the height in $FeTe_{1-x}Se_x$ by changing x to drive a topological phase transition, it is known that in the monolayer FeSe, the substrate can also affect the in-plane lattice constants and tune the Se height. For example, the measured lattice constant of FeSe on $SrTiO_3$ is about 3.82 Å [25] while the lattice constant is 3.99 Å in FeSe/Nb:$SrTiO_3$/$KTaO_3$ heterostructures [26]. Therefore, the nontrivial topology discussed here may also exist in the monolayer FeSe on a substrate. Even if the strength of SOC in iron pnictides is relatively weaker than those of iron chalcogenides, the coupling between Fe and anions can still create parity exchange. For bulk system, the parity exchange can happen at the Z point, which will drive the system into a strong topological phase.

The existence of nontrivial topology in $FeTe_{1-x}Se_x$ is supported by the recent experimental observation [27] in a bulk material. Zhang *et al.* observed an electron band above the Fermi level in $FeTe_{0.55}Se_{0.45}$ [27], which is rather similar to the band of FeTe with $a = 3.925$ Å. Furthermore, recently 1 UC FeSe/$SrTiO_3$ is found to lie in proximity to the topological phase transition [28]. It is also worth mentioning that a zero-bias peak (ZBP) was observed recently at an iron impurity site in the superconducting state of $FeTe_{1-x}Se_x$ [29]. The robustness of zero-energy bound state against magnetic field could support its closeness to nontrivial topology. However, no ZBP was observed at the impurity site in the FeSe material [30]. According to our calculations, the FeSe is topologically trivial but $FeTe_{1-x}Se_x$ ($x < 0.7$) is topologically nontrivial. Therefore, the ZBP is most likely to be related to the nontrivial topology discussed above. In experiments, the topological phase transition can be clearly seen by tracking the gap evolution at the Γ point with the increase of Te concentration in $FeTe_{1-x}Se_x$. The topologically protected one-dimensional nontrivial edge states, as shown in Fig. 5, can be detected in scanning tunneling microscopy experiments [31,32].

In conclusion, we predict that the monolayer and the thin film $FeTe_{1-x}Se_x$ is in a topological phase, which is induced by the parity exchange at the Γ point. The $FeTe_{1-x}Se_x$ can be an ideal system for realizing topological superconductors and Majorana fermions in a single phase.

Note added. Recently, we have learned that an independent study on the bulk band structure of $FeTe_{1-x}Se_x$ and its three-dimensional nontrivial topology is being carried out simultaneously with this work [33].

ACKNOWLEDGMENTS

We thank H. Ding for discussions. We thank X. Dai and Z. Fang for informing us of their related independent work on bulk FeTe(Se). The work is supported by the Ministry of Science and Technology of China 973 program (Grants No. 2012CV821400), National Science Foundation of China (Grants No. NSFC-1190024, No. 91536108, and No. 11104339), and the Strategic Priority Research Program of CAS (Grants No. XDB07000000 and No. XDB01010000).

APPENDIX A: PARITIES AT X AND M POINTS

Each band is fourfold degenerate at X and M points and includes two Kramers pairs, protected by the crystal symmetry. At the X $[k_X = (\pi,0)]$ point an eigenstate is $|\Phi(k_X)\rangle$ and

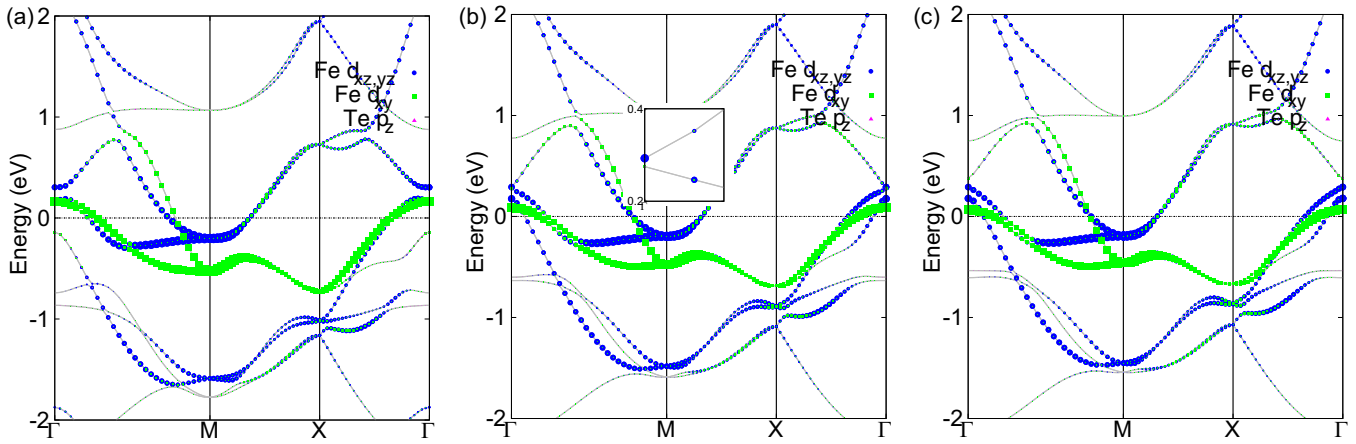

FIG. 6. The orbital characters of band structures from DFT with different lattice constants. (a) $a = 3.805$ Å, (b) $a = 3.9$ Å, and (c) $a = 3.925$ Å. The inset in (b) shows the bands near the Γ point.

$\hat{g}_2|\Phi(k_X)\rangle$ is also an eigenstate with the same energy at X. The products of $\hat{g}_2$ and $\hat{I}$ are

$$\hat{g}_2\hat{I} = \left\{C_{2X}\middle|\tfrac{1}{2}\tfrac{1}{2}\right\}, \tag{A1}$$

$$\hat{I}\hat{g}_2 = \left\{C_{2X}\middle|-\tfrac{1}{2}\tfrac{1}{2}\right\}, \tag{A2}$$

where C_{2X} is a twofold rotation around the X axis. Thus, $\hat{g}_2$ does not commute with $\hat{I}$ and $\hat{g}_2\hat{I}$ differs from $\hat{g}_2\hat{I}$ by a lattice vector translation. From the above equations, we have $\{\hat{g}_2, \hat{I}\} = 0$ at X. Therefore, the two states connected by $\hat{g}_2$ at X have opposite parities. Similar calculations show that $\{\hat{g}_1, \hat{I}\} = 0$ at the M point. The two Kramers pairs at the M point connected by $\hat{g}_2$ also have opposite parities.

APPENDIX B: ORBITAL CHARACTERS FOR MONOLAYER FeTe WITH DIFFERENT LATTICE CONSTANTS

Our DFT calculations employ the projector augmented wave (PAW) method encoded in the Vienna *ab initio* simulation package (VASP) [34–36], and the generalized-gradient approximation (GGA) [37] for the exchange correlation functional are used. The cutoff energy of 500 eV is taken for expanding the wave functions into plane-wave basis. In the calculation, the Brillouin zone is sampled in the **k** space within the Monkhorst-Pack scheme [38]. The number of these k points is $11 \times 11 \times 1$ for monolayer and bilayer FeTe. We relax the lattice constants and internal atomic positions and forces are minimized to less than 0.01 eV/Å in the relaxation. We used the maximally localized Wannier functions (MLWFs) to construct a tight binding model by fitting the DFT band structure, where 16 MLWFs are included.

The orbtial characters of DFT bands for FeTe with different lattice constants are shown in Fig. 6. The monolayer FeTe of $a = 3.805$ and $a = 3.9$ Å have inverted band structures, while the monolayer FeTe of $a = 3.925$ Å has a norm band. The band inversion in FeTe $a = 3.9$ Å is driven by spin-orbit coupling, as shown in the inset of Fig. 6(b). We have performed calculations with monolayer FeSe with $a = 3.805$ Å and $d = 1.59$ Å (no relaxation) and find that the band structure at Γ [see Fig. 7(a)] is rather similar to that of FeTe. The band inversion has happened. Therefore, in the main text, the main effect of Se concentration in $FeTe_{1-x}Se_x$ is modeled as the change of anion height. In iron pnictides LiFeAs, the parities at Γ and Z are shown in Fig. 7(b) and we find that band inversion happens at the Z point, which is induced by the interlayer coupling of As p_z and Fe d orbitals.

APPENDIX C: 16*dp* TIGHT BINDING MODEL

A general model including Fe d and X (X = Te,Se) p oribtals for iron-based superconductors can be written as

$$H_t = \sum_{\alpha\beta}\sum_{mn}\sum_{ij}\left(t^{mn}_{\alpha\beta,ij} + \epsilon_n\delta_{mn}\delta_{\alpha\beta}\delta_{ij}\right)c^{\dagger}_{\alpha m\sigma}(i)c_{\beta n\sigma}(j) \tag{C1}$$

Basically the primitive cell contains two Fe atoms in iron-based superconductors. To obtain the tight binding model in one-Fe unit cell, we need a particular gauge to unfold the band structure. To get this gauge, we need to find out which hopping terms break the translational symmetry in a one-Fe unit cell.

Consider the symmetry operation: the reflection across the xy plane σ_z and the in-plane translation by one Fe-Fe distance T. $R = \sigma_z T = \{\sigma_z|\frac{1}{2}\frac{1}{2}\}$ is the symmetry operation of the lattice for the iron-based superconductor. The Hamiltonian can be written as $H = H_{AA} + H_{BB} + H_{AB}$, where A and B denote the sublattices. We can classify the d and p orbitals according to eigenvalues of the operation σ_z into two groups: $\{d_{xz}, d_{yz}, p_z\} \in g_1$ and $\{d_{z^2}, d_{x^2-y^2}, d_{xy}, p_x, p_y\} \in g_2$, where the orbital basis is aligned parallel to the nearest-neighbor Fe-Fe direction. Consider the hopping term,

$$H_{ag_\alpha,bg_\beta} = \sum_{ij,\alpha\in g_\alpha,\beta\in g_\beta}(t_{ai,bj}c^{\dagger}_{ia\alpha}c_{jb\beta} + \text{H.c.}), \tag{C2}$$

where a and b are sublattice indices. Under the operation R, we have

$$RH_{ag_\alpha,bg_\beta}R^{\dagger} = (-1)^{\delta_{g_\alpha g_\beta}}\sum_{ij,\alpha\in g_\alpha,\beta\in g_\beta}(t_{ai,bj}c^{\dagger}_{i\bar{a}\alpha}c_{j\bar{b}\beta} + \text{H.c.}), \tag{C3}$$

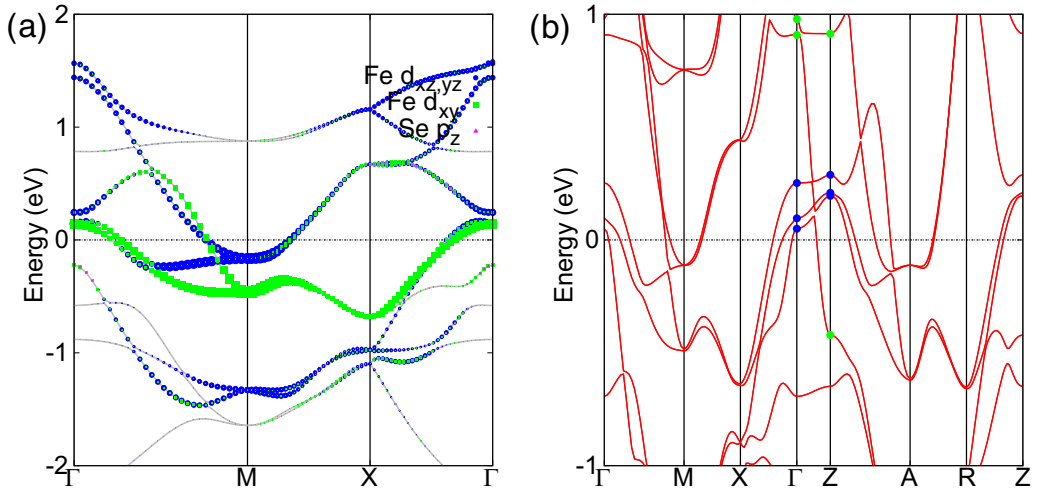

FIG. 7. (a) The orbital characters of band structures in FeSe with $a = 3.805$ and $d = 1.59$ Å. (b) The band structure of LiFeAs. The parities of the eigenstates at Γ and Z near the Fermi level are shown: blue circles for even parities and green circles for odd parities.

where $\bar{a}$ represents the opposite sublattice. If $g_\alpha = g_\beta$, $RH_{ag_\alpha,bg_\beta}R^\dagger = H_{\bar{a}g_\alpha,\bar{b}g_\beta}$ and this term preserves the translational symmetry of one Fe unit cell. If $g_\alpha \neq g_\beta$, however, there should be a minus sign after the operation, that is, $RH_{ag_\alpha,bg_\beta}R^\dagger = -H_{\bar{a}g_\alpha,\bar{b}g_\beta}$. It is the above hopping terms that break the translational symmetry of one iron unit cell. The origin of the minus sign is attributed to the σ_z operation on g_1 orbitals, $(d_{xz},d_{yz},p_z) \xrightarrow{\sigma_z} -(d_{xz},d_{yz},p_z)$. To obtain the Hamiltonian in one iron unit cell, we can choose an artificial gauge $(d_{xz},d_{yz},p_z) \xrightarrow{T} -(d_{xz},d_{yz},p_z)$, that is, the signs of orbitals in the g_1 group are opposite for A and B sublattices. With this gauge, $RH_{ag_\alpha,bg_\beta}R^\dagger = H_{\bar{a}g_\alpha,\bar{b}g_\beta}$ is satisfied and all the hopping terms preserve the translational symmetry of one Fe unit cell. Because only the intergroup hopping terms break the translation symmetry, we can also choose another gauge: $(d_{z^2},d_{xy},d_{x^2-y^2},p_x,p_y) \xrightarrow{T} -(d_{z^2},d_{xy},d_{x^2-y^2},p_x,p_y)$ and it can also ensure that the Hamiltonian is invariant under one Fe unit cell translation. In the artificial gauge, the intergroup hopping parameters and intragroup with gauge (g_1 or g_2) hopping parameters between sites separated by an odd number of lattice constants (one Fe lattice) are opposite to those in the natural gauge. In the following, we adopt the latter gauge.

The tight binding Hamiltonian in momentum space can be written as

$$H = \sum_{k\sigma} \phi^\dagger_\sigma(k) A(k) \phi_\sigma(k). \tag{C4}$$

Here, k is defined in the Brillioun zone of one Fe unit cell (BZ1). $\phi_\sigma(k) = [c_{xz\sigma}(k),c_{yz\sigma}(k),c_{x^2-y^2\sigma}(k+Q),c_{xy\sigma}(k+Q),c_{z^2\sigma}(k+Q),c_{x\sigma}(k+Q),c_{y\sigma}(k+Q),c_{z\sigma}(k)]^T$ with $Q = (\pi,\pi)$ defined in the BZ of one Fe unit cell. The matrix elements of $A(k)$ are given in the next part of Appendix C and the hopping parameters are given in Table II. The connection between the bases in the one-Fe unit cell and the two-Fe unit cell is

$$c_\alpha(k) = \frac{\sqrt{2}}{2}[c_{A\alpha}(q) + c_{B\alpha}(q)] \tag{C5}$$

$$c_\alpha(k+Q) = \frac{\sqrt{2}}{2}[c_{A\alpha}(q) - c_{B\alpha}(q)], \tag{C6}$$

where q is defined in the BZ of the two-Fe unit cell (BZ2). The on-site SOC Hamiltonian in momentum space reads

$$H_{so} = H_{sf} + H_{snf}, \tag{C7}$$

$$H_{snf} = \sum_{k\in BZ1} \frac{-i\sigma\lambda_1}{2} c^\dagger_{xz\sigma}(k) c_{yz\sigma}(k) + \sum_k i\sigma\lambda_1 c^\dagger_{xy\sigma}(k) c_{x^2-y^2\sigma}(k) + \sum_k \frac{-i\sigma\lambda_2}{2} c_{x\sigma}(k) c_{y\sigma}(k) + \text{H.c.}, \tag{C8}$$

$$\begin{aligned} H_{sf} = {} & \sum_k \frac{i\lambda_1}{2} c^\dagger_{xy\uparrow}(k)[-c_{xz\downarrow}(k) - ic_{yz\downarrow}(k)] + \frac{i\lambda_1}{2} c^\dagger_{xy\downarrow}(k)[-c_{xz\uparrow}(k) + ic_{yz\uparrow}(k)] \\ & + \frac{i\lambda_1}{2} c^\dagger_{x^2-y^2\uparrow}(k)[-ic_{xz\downarrow}(k) + c_{yz\downarrow}] + \frac{i\lambda_1}{2} c^\dagger_{x^2-y^2\downarrow}(k)[ic_{xz\uparrow}(k) + c_{yz\uparrow}(k)] \\ & + \frac{i\sqrt{3}\lambda_1}{2} c^\dagger_{z^2\uparrow}(k)[ic_{xz\downarrow}(k) + c_{yz\downarrow}(k)] + \frac{i\sqrt{3}\lambda_1}{2} c^\dagger_{z^2\downarrow}(k)[-ic_{xz\uparrow}(k) + c_{yz\uparrow}(k)] \\ & + \frac{i\lambda_2}{2} c^\dagger_{z\uparrow}(k)[ic_{x\downarrow}(k) + c_{y\downarrow}(k)] + \frac{i\lambda_2}{2} c^\dagger_{z\downarrow}(k)[-ic_{x\uparrow}(k) + c_{y\uparrow}(k)], \end{aligned} \tag{C9}$$

TABLE II. Hopping parameters to fit the DFT bands in the tight binding model for monolayer FeTe with $a = 3.805$ Å. The x direction is along the Fe-Fe bond. The on-site energies of the d and p oribtals are (all in eV): $\epsilon_1 = -0.723$, $\epsilon_3 = -1.082$, $\epsilon_4 = -0.766$, $\epsilon_5 = -0.980$, $\epsilon_6 = -2.417$, and $\epsilon_8 = -2.712$.

v	v_i^{mn}	$i = x$	$i = y$	$i = xy$	$i = xx$	$i = yy$	$i = xxy$	$i = xyy$	$i = xxyy$
	$mn = 11$	0.272	−0.043	0.043	−0.009	−0.007	−0.012	0.013	
	$mn = 33$	0.392		0.074	0.013				
	$mn = 44$	−0.297		−0.062	−0.007				
	$mn = 55$	0.159		−0.074	0.008		−0.008		
	$mn = 12$			0.020					
t	$mn = 13$		0.078						
	$mn = 14$	0.175		0.075					
	$mn = 15$		0.045	−0.062					
	$mn = 34$								
	$mn = 35$	−0.220							
	$mn = 45$			0.046					
	$mn = 11$			0.105			0.046	0.010	0.041
	$mn = 12$			0.722			0.019	−0.104	0.021
	$mn = 13$			0.134			0.066	−0.027	0.014
	$mn = 31$			−0.491			0.048	−0.028	
q	$mn = 33$							−0.016	
	$mn = 41$			0.067			−0.066	0.051	
	$mn = 43$			0.569				−0.014	−0.035
	$mn = 51$			0.303			−0.056		
	$mn = 53$			−0.472				0.010	
	$mn = 11$	−0.261	−0.175	0.340			0.014	−0.014	0.048
s	$mn = 33$	0.319		−0.042	−0.009			−0.023	
	$mn = 12$			0.511					
	$mn = 13$	−0.367							

where σ labels spin and λ_1 and λ_2 are the parameters of SOC for Fe and Te. H_{sp} and H_{snp} are the spin-flip and nonflip terms in SOC, respectively. The Hamiltonian of the FeTe system is

$$H = H_t + H_{so} = \sum_{k \in BZ1} \Psi^\dagger(k) B(k) \Psi(k), \tag{C10}$$

where $\Psi(k) = [\phi_\uparrow^T(k), \phi_\uparrow^T(k+Q), \phi_\downarrow^T(k), \phi_\downarrow^T(k+Q)]^T$. The Hamiltonian matrix $B(k)$ is

$$B(k) = \begin{pmatrix} A(k) + h_{snf}(k) & 0 & 0 & h_{sp}(k) \\ 0 & A(k+Q) + h_{snf}(k+Q) & h_{sp}(k+Q) & 0 \\ 0 & h_{sp}^\dagger(k+Q) & A(k) - h_{snf}(k) & 0 \\ h_{sp}^\dagger(k) & 0 & 0 & A(k+Q) - h_{snf}(k+Q) \end{pmatrix}. \tag{C11}$$

Here, $h_{snp}(k)$ and $h_{sp}(k)$ have the form

$$h_{snp}(k) = \begin{pmatrix} 0 & -\frac{i\lambda_1}{2} & 0 & 0 & 0 & 0 & 0 & 0 \\ \frac{i\lambda_1}{2} & 0 & 0 & 0 & 0 & 0 & 0 & 0 \\ 0 & 0 & 0 & -i\lambda_1 & 0 & 0 & 0 & 0 \\ 0 & 0 & i\lambda_1 & 0 & 0 & 0 & 0 & 0 \\ 0 & 0 & 0 & 0 & 0 & 0 & 0 & 0 \\ 0 & 0 & 0 & 0 & 0 & 0 & -\frac{i\lambda_2}{2} & 0 \\ 0 & 0 & 0 & 0 & 0 & \frac{i\lambda_2}{2} & 0 & 0 \\ 0 & 0 & 0 & 0 & 0 & 0 & 0 & 0 \end{pmatrix}, \tag{C12}$$

$$h_{sp}(k)=\begin{pmatrix} 0 & 0 & -\frac{\lambda_1}{2} & \frac{i\lambda_1}{2} & \frac{\sqrt{3}\lambda_1}{2} & 0 & 0 & 0 \\ 0 & 0 & -\frac{i\lambda_1}{2} & -\frac{\lambda_1}{2} & -\frac{i\sqrt{3}\lambda_1}{2} & 0 & 0 & 0 \\ \frac{\lambda_1}{2} & \frac{i\lambda_1}{2} & 0 & 0 & 0 & 0 & 0 & 0 \\ -\frac{i\lambda_1}{2} & \frac{\lambda_1}{2} & 0 & 0 & 0 & 0 & 0 & 0 \\ -\frac{\sqrt{3}\lambda_1}{2} & \frac{i\sqrt{3}\lambda_1}{2} & 0 & 0 & 0 & 0 & 0 & 0 \\ 0 & 0 & 0 & 0 & 0 & 0 & 0 & \frac{\lambda_2}{2} \\ 0 & 0 & 0 & 0 & 0 & 0 & 0 & \frac{-i\lambda_2}{2} \\ 0 & 0 & 0 & 0 & 0 & -\frac{\lambda_2}{2} & \frac{i\lambda_2}{2} & 0 \end{pmatrix}. \tag{C13}$$

The matrix elements of $A(k)$

a. d-d hopping terms

For d orbitals the matrix elements are
(a) intraorbital terms:

$$\xi_{11/22}=\epsilon_1+2t_{x/y}^{11}\cos k_x+2t_{y/x}^{11}\cos k_y+4t_{xy}^{11}\cos k_x\cos k_y+2t_{xx/yy}^{11}\cos 2k_x+2t_{yy/xx}^{11}\cos 2k_y+4t_{xxy/xyy}^{11}\cos 2k_x\cos k_y$$
$$+4t_{xyy/xxy}^{11}\cos k_x\cos 2k_y+4t_{xxyy}^{11}\cos 2k_x\cos 2k_y, \tag{C14}$$

$$\xi_{33}=\epsilon_3+2t_x^{33}(\cos k_x+\cos k_y)+4t_{xy}^{33}\cos k_x\cos k_y+2t_{xx}^{33}(\cos 2k_x+\cos 2k_y)+4t_{xxyy}^{33}\cos 2k_x\cos 2k_y \tag{C15}$$

$$\xi_{44}=\epsilon_4+2t_x^{44}(\cos k_x+\cos k_y)+4t_{xy}^{44}\cos k_x\cos k_y+2t_{xx}^{44}(\cos 2k_x+\cos 2k_y)+4t_{xxy}^{44}(\cos 2k_x\cos k_y+\cos k_x\cos 2k_y),$$
$$+4t_{xxyy}^{44}\cos 2k_x\cos 2k_y, \tag{C16}$$

$$\xi_{55}=\epsilon_5+2t_x^{55}(\cos k_x+\cos k_y)+4t_{xy}^{55}\cos k_x\cos k_y+2t_{xx}^{55}(\cos 2k_x+\cos 2k_y)+4t_{xxy}^{55}(\cos 2k_x\cos k_y+\cos k_x\cos 2k_y)$$
$$+4t_{xxyy}^{55}\cos 2k_x\cos 2k_y; \tag{C17}$$

(b) interorbital terms:

$$\xi_{12}=-4t_{xy}^{12}\sin k_x\sin k_y-4t_{xxy}^{12}(\sin 2k_x\sin k_y+\sin k_x\sin 2k_y)-4t_{xxyy}^{12}\sin 2k_x\sin 2k_y, \tag{C18}$$

$$\xi_{13/23}=\pm 2it_y^{13}\sin k_{y/x}\pm 4it_{xy}^{13}\sin k_{y/x}\cos k_{x/y}\pm 2it_{yy}^{13}\sin 2k_{y/x}\pm 4it_{xxy}^{13}\sin k_{y/x}\cos 2k_{x/y}\pm 4it_{xyy}^{13}\sin 2k_{y/x}\cos k_{x/y}$$
$$\pm 4it_{xxyy}^{13}\sin 2k_{y/x}\cos 2k_{x/y}, \tag{C19}$$

$$\xi_{14/24}=2it_x^{14}\sin k_{x/y}+4it_{xy}^{14}\cos k_{y/x}\sin k_{x/y}+2it_{xx}^{14}\sin 2k_{x/y}+4it_{xxy}^{14}\sin 2k_{x/y}\cos k_{y/x}$$
$$+4it_{xxyy}^{14}\sin 2k_{x/y}\cos 2k_{y/x}, \tag{C20}$$

$$\xi_{15/25}=2it_y^{15}\sin k_{y/x}+4it_{xy}^{15}\cos k_{x/y}\sin k_{y/x}+2it_{yy}^{15}\sin 2k_{y/x}+4it_{xxy}^{15}\cos 2k_{x/y}\sin k_{y/x}+4it_{xyy}^{15}\cos k_{x/y}\sin 2k_{y/x}$$
$$+4it_{xxyy}^{15}\cos 2k_{x/y}\sin 2k_{y/x}, \tag{C21}$$

$$\xi_{34}=-4t_{xxy}^{34}(\sin 2k_x\sin k_y-\sin k_x\sin 2k_y), \tag{C22}$$

$$\xi_{35}=2t_x^{35}(\cos k_x-\cos k_y)+4t_{xxy}^{35}(\cos 2k_x\cos k_y-\cos k_x\cos 2k_y)+2t_{xx}^{35}(\cos 2k_x-\cos 2k_y), \tag{C23}$$

$$\xi_{45}=-4t_{xy}^{45}\sin k_x\sin k_y-4t_{xxy}^{45}(\sin 2k_x\sin k_y+\sin k_x\sin 2k_y)-4t_{xxyy}^{45}\sin 2k_x\sin 2k_y. \tag{C24}$$

b. p-p hopping terms

For p orbitals the matrix elements are
(a) intraorbital terms:

$$\xi_{66/77}=\epsilon_6+2s_x^{11}\cos k_{x/y}+2s_y^{11}\cos k_{y/x}+4s_{xy}^{11}\cos k_{x/y}\cos k_{y/x}+4s_{xxy}^{11}\cos 2k_{x/y}\cos k_{y/x}$$
$$+4s_{xyy}^{11}\cos k_{x/y}\cos 2k_{y/x}+4s_{xxyy}^{11}\cos 2k_{x/y}\cos 2k_{y/x}, \tag{C25}$$

$$\xi_{88}=\epsilon_8+2s_x^{33}(\cos k_x+\cos k_y)+4s_{xy}^{33}\cos k_x\cos k_y+2s_{xx}^{33}(\cos 2k_x+\cos 2k_y)+4s_{xyy}^{33}(\cos k_x\cos 2k_y+\cos 2k_x\cos k_y); \tag{C26}$$

(b) interorbital terms:

$$\xi_{67}=-4s_{xy}^{12}\sin k_x\sin k_y, \tag{C27}$$

$$\xi_{68/78}=2is_x^{13}\sin k_{x/y}. \tag{C28}$$

c. d-p hopping terms

The matrix elements between d and p orbitals are

$$\xi_{16/27} = 4q_{xy}^{11}\cos\left(\tfrac{1}{2}k_{x/y}\right)\cos\left(\tfrac{1}{2}k_{y/x}\right) + 4q_{xyy}^{11}\cos\left(\tfrac{1}{2}k_{x/y}\right)\cos\left(\tfrac{3}{2}k_{y/x}\right) + 4q_{xxy}^{11}\cos\left(\tfrac{3}{2}k_{x/y}\right)\cos\left(\tfrac{1}{2}k_{y/x}\right) + 4q_{xxyy}^{11}\cos\left(\tfrac{3}{2}k_{x/y}\right)\cos\left(\tfrac{3}{2}k_{y/x}\right), \tag{C29}$$

$$\xi_{17/26} = -4q_{xy}^{12}\sin\left(\tfrac{1}{2}k_{x/y}\right)\sin\left(\tfrac{1}{2}k_{y/x}\right) + 4q_{xyy}^{12}\sin\left(\tfrac{1}{2}k_{x/y}\right)\sin\left(\tfrac{3}{2}k_{y/x}\right) + 4q_{xxy}^{12}\sin\left(\tfrac{3}{2}k_{x/y}\right)\sin\left(\tfrac{1}{2}k_{y/x}\right) - 4q_{xxyy}^{12}\sin\left(\tfrac{3}{2}k_{x/y}\right)\sin\left(\tfrac{3}{2}k_{y/x}\right), \tag{C30}$$

$$\xi_{18/28} = 4iq_{xy}^{13}\sin\left(\tfrac{1}{2}k_{x/y}\right)\cos\left(\tfrac{1}{2}k_{y/x}\right) - 4iq_{xyy}^{13}\sin\left(\tfrac{1}{2}k_{x/y}\right)\cos\left(\tfrac{3}{2}k_{y/x}\right) + 4iq_{xxy}^{13}\sin\left(\tfrac{3}{2}k_{x/y}\right)\cos\left(\tfrac{1}{2}k_{y/x}\right) + 4iq_{xxyy}^{13}\sin\left(\tfrac{3}{2}k_{x/y}\right)\cos\left(\tfrac{3}{2}k_{y/x}\right), \tag{C31}$$

$$\xi_{36/37} = \pm 4iq_{xy}^{31}\cos\left(\tfrac{1}{2}k_{x/y}\right)\sin\left(\tfrac{1}{2}k_{y/x}\right) \pm 4iq_{xyy}^{31}\cos\left(\tfrac{1}{2}k_{x/y}\right)\sin\left(\tfrac{3}{2}k_{y/x}\right) \mp 4iq_{xxy}^{31}\cos\left(\tfrac{3}{2}k_{x/y}\right)\sin\left(\tfrac{1}{2}k_{y/x}\right), \tag{C32}$$

$$\xi_{38} = 4q_{xyy}^{33}\left[\sin\left(\tfrac{1}{2}k_x\right)\sin\left(\tfrac{3}{2}k_y\right) - \sin\left(\tfrac{3}{2}k_x\right)\sin\left(\tfrac{1}{2}k_y\right)\right], \tag{C33}$$

$$\xi_{46/47} = 4iq_{xy}^{41}\sin\left(\tfrac{1}{2}k_{x/y}\right)\cos\left(\tfrac{1}{2}k_{y/x}\right) - 4iq_{xyy}^{41}\sin\left(\tfrac{1}{2}k_{x/y}\right)\cos\left(\tfrac{3}{2}k_{y/x}\right) + 4iq_{xxy}^{41}\sin\left(\tfrac{3}{2}k_{x/y}\right)\cos\left(\tfrac{1}{2}k_{y/x}\right), \tag{C34}$$

$$\xi_{48} = 4q_{xy}^{43}\cos\left(\tfrac{1}{2}k_x\right)\cos\left(\tfrac{1}{2}k_y\right) + 4q_{xyy}^{43}\left[\cos\left(\tfrac{1}{2}k_x\right)\cos\left(\tfrac{3}{2}k_y\right) + \cos\left(\tfrac{3}{2}k_x\right)\cos\left(\tfrac{1}{2}k_y\right)\right] + 4q_{xxyy}^{43}\cos\left(\tfrac{3}{2}k_x\right)\cos\left(\tfrac{3}{2}k_y\right), \tag{C35}$$

$$\xi_{56/57} = 4iq_{xy}^{51}\cos\left(\tfrac{1}{2}k_{x/y}\right)\sin\left(\tfrac{1}{2}k_{y/x}\right) + 4iq_{xyy}^{51}\cos\left(\tfrac{1}{2}k_{x/y}\right)\sin\left(\tfrac{3}{2}k_{y/x}\right) - 4iq_{xxy}^{51}\cos\left(\tfrac{3}{2}k_{x/y}\right)\sin\left(\tfrac{1}{2}k_{y/x}\right), \tag{C36}$$

$$\xi_{58} = -4q_{xy}^{53}\sin\left(\tfrac{1}{2}k_x\right)\sin\left(\tfrac{1}{2}k_y\right) + 4q_{xyy}^{53}\left[\sin\left(\tfrac{1}{2}k_x\right)\sin\left(\tfrac{3}{2}k_y\right) + \sin\left(\tfrac{3}{2}k_x\right)\sin\left(\tfrac{1}{2}k_y\right)\right] \tag{C37}$$

APPENDIX D: EFFECTIVE MODELS AROUND Γ POINT

From the DFT band structure of FeTe, we find that the states at the Γ point near the Fermi level are mainly attributed to Fe d_{xz}, d_{yz}, d_{xy} and Te p_x, p_y, p_z orbitals; hence we focus on these states and neglect the others. When considering SOC, it is convenient to transform the atomic orbitals to harmonic oribtals with definite oribtal angular momentum,

$$c_{2\pm1,\sigma}(k) = \mp\frac{1}{\sqrt{2}}[c_{xz\sigma}(k) \pm ic_{yz\sigma}(k)], \tag{D1}$$

$$c_{1\pm1,\sigma}(k) = \mp\frac{1}{\sqrt{2}}[c_{x\sigma}(k) \pm ic_{y\sigma}(k)]. \tag{D2}$$

At the Γ point, d_{xz} orbitals can only couple with p_x and d_{yz} with p_y and d_{xy} with p_z. At the Γ point, the effective Hamiltonian in the basis of $[c_{21,\sigma}(k), c_{11,\sigma}(k+Q), c_{2-1,\sigma}(k), c_{1-1,\sigma}(k+Q), c_{xy,\sigma}(k+Q), c_{z,\sigma}(k)]$ is

$$H_1 = \begin{pmatrix} \epsilon_{xz}+\sigma\lambda_1/2 & t_\Gamma & 0 & 0 & 0 & 0 \\ t_\Gamma & \epsilon_x+\sigma\lambda_2/2 & 0 & 0 & 0 & 0 \\ 0 & 0 & \epsilon_{xz}-\sigma\lambda_1/2 & t_\Gamma & 0 & 0 \\ 0 & 0 & t_\Gamma & \epsilon_x-\sigma\lambda_2/2 & 0 & 0 \\ 0 & 0 & 0 & 0 & \epsilon_{xy} & t'_\Gamma \\ 0 & 0 & 0 & 0 & t'_\Gamma & \epsilon_z \end{pmatrix}. \tag{D3}$$

The matrix is block diagonal and the eigenvalues are

$$E_{1\sigma}^{\pm} = \frac{a_1+b_1 \pm \sqrt{(a_1-b_1)^2+4t_\Gamma^2}}{2}, \tag{D4}$$

$$E_{2\sigma}^{\pm} = \frac{a_2+b_2 \pm \sqrt{(a_2-b_2)^2+4t_\Gamma^2}}{2}, \tag{D5}$$

$$E_{0\sigma}^{\pm} = \frac{\epsilon_{xy}+\epsilon_z \pm \sqrt{(\epsilon_{xy}-\epsilon_z)^2+4t_\Gamma'^2}}{2}, \tag{D6}$$

TABLE III. Parameters in the six-band effective model for monolayer FeTe with different lattice constants. The units of C_n, A_n and D_n, B_n are eV, eV Å, eV Å^2.

Lattice (Å)	C_1	C_3	C_4	D_1	D_2	B_2	D_3	D_4	A_1	A_2
3.805	0.303	0.167	−0.140	−4.212	0.222	0.300	−2.294	0.884	1.475	1.744
3.9	0.293	0.176	0.275	−4.175	0.715	0.212	−2.879	−0.152	1.467	1.701
3.925	0.291	0.179	0.381	−4.077	−0.843	0.078	−3.167	−0.321	1.494	1.642

where $a_{1/2} = \epsilon_{xz} \pm \sigma\lambda_1/2$ and $b_{1/2} = \epsilon_x \pm \sigma\lambda_2/2$. The corresponding eigenvectors are

$$\begin{pmatrix}\alpha^{\pm}_{1\sigma}\\ \beta^{\pm}_{1\sigma}\end{pmatrix} = \frac{1}{N_{1\pm}}\begin{pmatrix}E^{\pm}_{1\sigma} - \epsilon_x - \sigma\lambda_2/2\\ t_\Gamma\end{pmatrix}, \tag{D7}$$

$$\begin{pmatrix}\alpha^{\pm}_{2\sigma}\\ \beta^{\pm}_{2\sigma}\end{pmatrix} = \frac{1}{N_{2\pm}}\begin{pmatrix}E^{\pm}_{2\sigma} - \epsilon_x + \sigma\lambda_2/2\\ t_\Gamma\end{pmatrix}, \tag{D8}$$

$$\begin{pmatrix}\alpha^{\pm}_{3\sigma}\\ \beta^{\pm}_{3\sigma}\end{pmatrix} = \frac{1}{N_{3\pm}}\begin{pmatrix}E^{\pm}_{3\sigma} - \epsilon_z\\ t_\Gamma\end{pmatrix}. \tag{D9}$$

Here, $N_{1,2,3\pm}$ are the normalization factors. Now, we define a new basis,

$$c_{1\pm,\sigma}(k) = \alpha^{\pm}_{1\sigma}c_{21,\sigma}(k) + \beta^{\pm}_{1\sigma}c_{11,\sigma}(k+Q), \tag{D10}$$

$$c_{-1\pm,\sigma}(k) = \alpha^{\pm}_{2\sigma}c_{2-1,\sigma}(k) + \beta^{\pm}_{2\sigma}c_{1-1,\sigma}(k+Q), \tag{D11}$$

$$c_{0\pm,\sigma}(k) = \alpha^{\pm}_{3\sigma}c_{xy,\sigma}(k+Q) + \beta^{\pm}_{3\sigma}c_{z,\sigma}(k), \tag{D12}$$

with $\alpha^{\pm}_{1\pm} = \alpha^{\pm}_{2\mp}$, $\beta^{\pm}_{1\pm} = \beta^{\pm}_{2\mp}$, $\alpha^{-}_{1,2\pm} = \beta^{+}_{1,2\pm}$, and $\beta^{-}_{1,2\pm} = -\alpha^{+}_{1,2\pm}$. Let $\alpha_1 = \alpha^{+}_{1+}$, $\alpha_2 = \alpha^{+}_{1-}$, $\beta_1 = \beta^{+}_{1+}$, $\beta_2 = \beta^{+}_{1-}$, $\gamma = \alpha^{+}_{3+}$, and $\delta = \beta^{+}_{3+}$, the new basis is $\tilde{\phi}_\sigma(k) = [c_{1+,\sigma}(k), c_{-1+,\sigma}(k), c_{x^2-y^2,\sigma}(k+Q), c_{0+,\sigma}(k), c_{z^2,\sigma}, c_{1-,\sigma}(k), c_{-1-,\sigma}(k), c_{0-,\sigma}(k)]^T$ and $\tilde{\phi}_\sigma(k) = U\phi_\sigma(k)$, where the unitary matrix U is given by

$$U = \begin{pmatrix}
-\frac{\alpha_1}{\sqrt{2}} & -\frac{\alpha_1}{\sqrt{2}}i & 0 & 0 & 0 & -\frac{\beta_1}{\sqrt{2}} & -\frac{\beta_1}{\sqrt{2}}i & 0\\
\frac{\alpha_2}{\sqrt{2}} & -\frac{\alpha_2}{\sqrt{2}}i & 0 & 0 & 0 & \frac{\beta_2}{\sqrt{2}} & -\frac{\beta_2}{\sqrt{2}}i & 0\\
0 & 0 & 1 & 0 & 0 & 0 & 0 & 0\\
0 & 0 & 0 & \gamma & 0 & 0 & 0 & \delta\\
0 & 0 & 0 & 0 & 1 & 0 & 0 & 0\\
-\frac{\beta_1}{\sqrt{2}} & -\frac{\beta_1}{\sqrt{2}}i & 0 & 0 & 0 & \frac{\alpha_1}{\sqrt{2}} & \frac{\alpha_1}{\sqrt{2}}i & 0\\
\frac{\beta_2}{\sqrt{2}} & -\frac{\beta_2}{\sqrt{2}}i & 0 & 0 & 0 & -\frac{\alpha_2}{\sqrt{2}} & \frac{\alpha_2}{\sqrt{2}}i & 0\\
0 & 0 & 0 & \delta & 0 & 0 & 0 & -\gamma
\end{pmatrix}. \tag{D13}$$

In the new basis $\tilde{\Psi}(k) = [\tilde{\phi}^T_\uparrow(k), \tilde{\phi}^T_\uparrow(k+Q), \tilde{\phi}^T_\downarrow(k), \tilde{\phi}^T_\downarrow(k+Q)]^T$ the Hamiltonian can be rewritten as

$$H = \sum_k \tilde{\Psi}^\dagger(k)\tilde{B}(k)\tilde{\Psi}(k), \tag{D14}$$

$$\tilde{B}(k) = \begin{pmatrix}
\tilde{A}(k) + \tilde{h}_{snf}(k) & 0 & 0 & \tilde{h}_{sp}(k)\\
0 & \tilde{A}(k+Q) + \tilde{h}_{snf}(k+Q) & \tilde{h}_{sp}(k+Q) & 0\\
0 & \tilde{h}^\dagger_{sp}(k+Q) & \tilde{A}(k) - h_{snf}(k) & 0\\
\tilde{h}^\dagger_{sp}(k) & 0 & 0 & \tilde{A}(k+Q) - \tilde{h}_{snf}(k+Q)
\end{pmatrix}. \tag{D15}$$

From the DFT band, we find that the band inversion happens in the "k" bands and we focus on the "k" bands near the Fermi level in the following. In the basis $\Psi_{\rm eff}(k) = [c_{1+,\uparrow}(k), c_{-1+,\uparrow}(k), c_{0+,\uparrow}(k), c_{-1+,\downarrow}(k), c_{1+,\downarrow}(k), c_{0+,\downarrow}(k)]$, we can get the effective model around the Γ point as

$$H_{\rm eff} = \sum_k \Psi^\dagger_{\rm eff}(k)h_{\rm eff}(k)\Psi_{\rm eff}(k), \tag{D16}$$

$$h_{\rm eff}(k) = \begin{pmatrix}h_1(k) & 0\\ 0 & h^\star_1(-k)\end{pmatrix}. \tag{D17}$$

The $h_1(k)$ has the following form:

$$h_1(k) = \begin{pmatrix}
D_1\left(k_x^2+k_y^2\right) + C_1 & D_2\left(k_x^2-k_y^2\right) + iB_2k_xk_y & A_1k_+\\
D_2\left(k_x^2-k_y^2\right) - iB_2k_xk_y & D_3\left(k_x^2+k_y^2\right) + C_3 & A_2k_-\\
A_1k_+ & A_2k_- & D_4\left(k_x^2+k_y^2\right) + C_4
\end{pmatrix}. \tag{D18}$$

The fitting parameters for different lattice constants are given in Table III and the corresponding bands are shown in Fig. 8. The bands of this effective model fit well with those of DFT around the Γ point. As $E^+_{1\uparrow} > E^-_{-1\uparrow}$, we can neglect the states with energies $E^-_{-1\uparrow}$. In the new basis $\tilde{\Psi}_{\rm eff}(k) = [c_{1+,\uparrow}(k), c_{0+,\uparrow}(k), c_{-1+,\downarrow}(k), c_{0+,\downarrow}(k)]$, the four-band effective

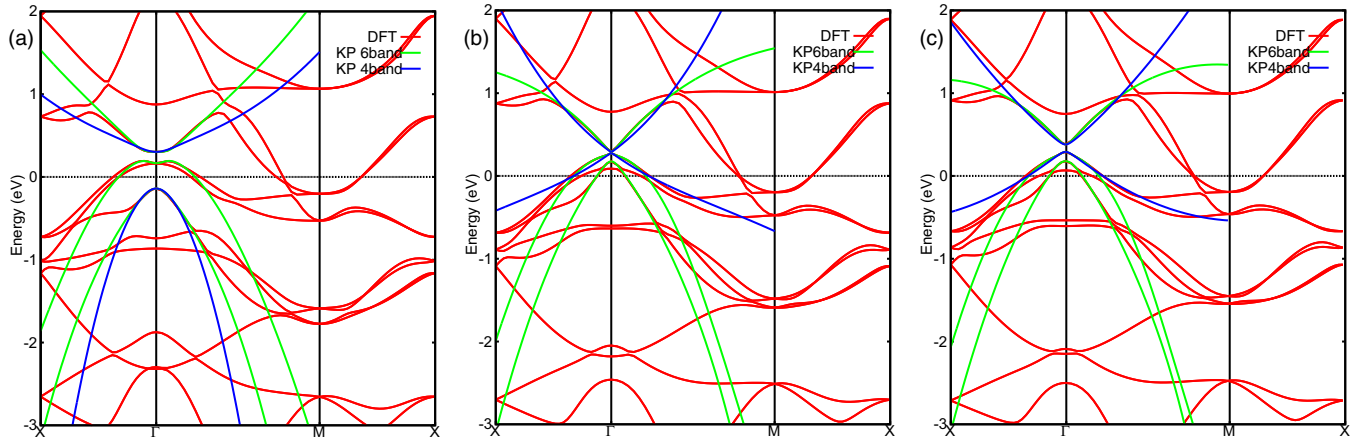

FIG. 8. Band structures from DFT and effective models for monolayer FeTe with different lattice constants. (a) $a = 3.805$ Å, (b) $a = 3.9$ Å, and (c) $a = 3.925$ Å. The red lines represent DFT band. The green and blue lines represent bands from six-band and four-band effective models, respectively.

Hamiltonian reads

$$H_{\text{eff}} = \sum_k \tilde{\Psi}^{\dagger}_{\text{eff}}(k)\tilde{h}_{\text{eff}}(k)\tilde{\Psi}_{\text{eff}}(k), \tag{D19}$$

$$\tilde{h}_{\text{eff}}(k) = \epsilon_0(k) + \begin{pmatrix} -M(k) & Ak_+ & 0 & 0 \\ Ak_- & M(k) & 0 & 0 \\ 0 & 0 & -M(k) & -Ak_- \\ 0 & 0 & -Ak_+ & M(k) \end{pmatrix}, \tag{D20}$$

where $\epsilon_k = C - D(k_x^2 + k_y^2)$, $M(k) = M - B(k_x^2 + k_y^2)$, and $k_\pm = k_x \pm ik_y$. $M < 0$ corresponds to the inverted regime, whereas $M > 0$ corresponds to the normal regime. The fitting parameters for different lattice constants are given in Table I in the main text and the corresponding bands are given in Fig. 8. $M < 0$ for lattice constant $a = 3.9$ and $a = 3.805$ Å, which indicates that the systems are topologically nontrivial.

APPENDIX E: ELECTRONIC STRUCTURES AND Z_2 TOPOLOGICAL NUMBERS FOR MULTILAYER FeTe

The band structure of bilayer FeTe is shown in Fig. 9(a). The parities of states near the Fermi level are shown in Fig. 9(a) and the oribtal characters are shown in Fig. 9(b). For the bilayer system, the inversion center is in the middle of the two layers. Therefore, $Ic_{\alpha,u}(k) = c_{\alpha,b}(-k)$ and $Ic_{\alpha,u}(k+Q) = -c_{\alpha,b}(-k+Q)$ for $\alpha = d$ orbitals and $Ic_{\alpha,u}(k) = -c_{\alpha,b}(-k)$ and $Ic_{\alpha,u}(k+Q) = c_{\alpha,b}(-k+Q)$ for $\alpha = p$ orbitals, where u and b are the layer indices. Because of the interlayer coupling, the number of states near the Fermi level doubles compared with the case of monolayer FeTe. The antibonding states with odd parity have high energies. The A_{2u} state contributed by d_{xy} and p_z have a strong interlayer coupling, leading to a large separation between A_{2u}^- and A_{2u}^+. Similar to the monolayer case, the system is topologically trivial if A_{2u}^+ and A_{2u}^- states are above the $E_{g\pm}^-$ state. However, in bilayer FeTe with $a = 3.809$ Å, A_{2u}^+ sinks below the $E_{g\pm}^-$ states, as shown in Fig. 9. Now, the parity exchange happens and the system is topologically nontrivial.

Figure 10 shows the band structure of trilayer FeTe. According to the parities shown in Fig. 10(a), we find that band inversion happens twice at the Γ point. Therefore, the trilayer FeTe is in a topologically trivial phase. Moreover, we have found that the quad-layer FeTe is topologically nontrivial. From the above calculation, in the multilayer FeTe case, the in-plane lattice constant, spin-orbit coupling, and interlayer

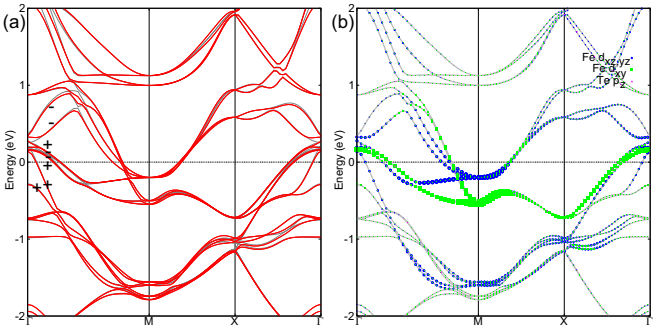

FIG. 9. Band structure and orbital characters from DFT for bilayer FeTe with $a = 3.809$ Å. (a) The red and gray lines denote the bands with SOC and without SOC. (b) The orbital characters of band structure near the Fermi level.

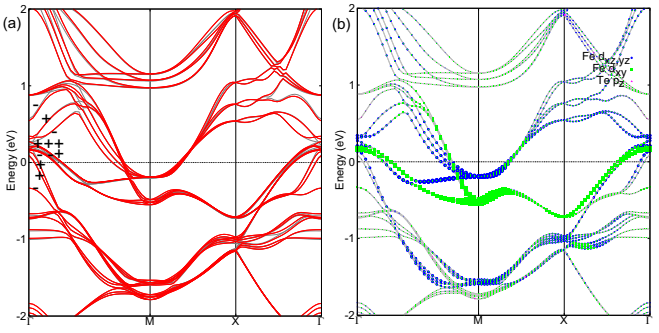

FIG. 10. Band structure and orbital characters from DFT for trilayer FeTe with $a = 3.812$ Å. (a) The red and gray lines denote the bands with SOC and without SOC. (b) The orbital characters of band structure near the Fermi level.

coupling are essential to the band inversion. The Z_2 topological number is oscillating with the number of FeTe layers.

This oscillation can be understood by a simple model. As A_{2u} states are attributed to Fe d_{xy} and Te p_z and E_g are attributed to Fe d_{xz},d_{yz} and Te p_x,p_y, we can roughly omit the interlayer coupling between E_g states and only consider the interlayer coupling J between A_{2u} states in multilayer FeTe. In N multilayer FeTe, the Hamiltonian for the A_{2u} states at the Γ point is given by the $N \times N$ matrix,

$$H_{A_{2u}} = \begin{pmatrix} \epsilon_{A_{2u}} & J & & & \\ J & \epsilon_{A_{2u}} & J & & \\ & J & \epsilon_{A_{2u}} & J & \\ & & \ddots & \ddots & \ddots \end{pmatrix}, \quad \text{(E1)}$$

where $\epsilon_{A_{2u}}$ is the energy of the A_{2u} state at the Γ point in monolayer FeTe. The eigenvalues of $H_{A_{2u}}$ are $E_k = \epsilon_{A_{2u}} + 2J\cos(\frac{k\pi}{N+1})$ $(k = 1,2,\ldots,N)$. Let Δ be the gap between the A_{2u} and E_{g-} states in monolayer FeTe; the A_{2u},k state is occupied in the multilayer system if $E_k - \epsilon_{A_{2u}} < \Delta$. Therefore, the number of band inversions at the Γ point is just the number of occupied A_{2u} states. The system is topologically nontrivial with odd number of band inversions and trivial with an even number of band inversions. The energies of A_{2u} states in multilayer FeTe are given in Table IV. Δ is estimated to be $0.9J$ and we find that band inversion happens once, twice, and three times for bilayer, trilayer, and tetralayer FeTe, respectively. It is consistent with our DFT calculations. By this simple model, we can also show that the Z_2 topological number is oscillating with the number of FeTe layers.

TABLE IV. Eigenenergies of A_{2u} states, number of band inversions, and Z_2 topological invariant in multilayer FeTe. $N_{A_{2u}}$ represents the number of band inversions. The energies are given in J.

Number of layers	Eigenenergies	$N_{A_{2u}}$	Z_2
2	±1.0	1	odd
3	±1.41, 0	2	even
4	±1.62, ±0.62	3	odd
5	±1.73, ±1.0, 0	3	odd
6	±1.80, ±1.24, ±0.45	4	even
7	±1.85, ±1.41, ±0.77, 0	5	odd
8	±1.88, ±1.53, ±1.0, ±0.35	5	odd
9	±1.90, ±1.62, ±1.18, ±0.62, 0	6	even
10	±1.92, ±1.68, ±1.31, ±0.83 ±0.28	7	odd

APPENDIX F: THE EFFECT OF Se DOPING IN $FeTe_{1-x}Se_x$

The substitution of Te atoms within FeTe with Se can kill the magnetic order and induce superconductivity. This substitution is mainly tuning the anion height and lattice constants, which are consistent with experiments (see Fig. 1 E and Fig. S6 in Ref. [19]). This isovalent substitution does not change the number of electrons and, in many ways, can be viewed as a chemical pressure in the system. As for the impurity effect from Se doping, it may affect the T_c of the system but should have little effect on the discussed topological properties, because they are protected by the time-reversal symmetry against weak nonmagnetic impurities or disorders.

[1] C. L. Kane and E. J. Mele, Phys. Rev. Lett. **95**, 226801 (2005).
[2] M. Z. Hasan and C. L. Kane, Rev. Mod. Phys. **82**, 3045 (2010).
[3] X.-L. Qi and S.-C. Zhang, Rev. Mod. Phys. **83**, 1057 (2011).
[4] Y. Kamihara, T. Watanabe, M. Hirano, and H. Hosono, J. Am. Chem. Soc. **130**, 3296 (2008).
[5] D. C. Johnston, Adv. Phys. **59**, 803 (2010).
[6] L. Fu and C. L. Kane, Phys. Rev. Lett. **100**, 096407 (2008).
[7] J. Linder, Y. Tanaka, T. Yokoyama, A. Sudbo, and N. Nagaosa, Phys. Rev. Lett. **104**, 067001 (2010).
[8] N. N. Hao and J. P. Hu, Phys. Rev. X **4**, 031053 (2014).
[9] X. X. Wu, C. C. Le, Y. Liang, S. S. Qin, H. Fan, and J. P. Hu, Phys. Rev. B **89**, 205102 (2014).
[10] X. X. Wu, S. S. Qin, Y. Liang, C. C. Le, H. Fan, and J. P. Hu, Phys. Rev. B **91**, 081111(R) (2015).
[11] K. Liu, Z. Y. Lu, and T. Xiang, Phys. Rev. B **85**, 235123 (2012).
[12] T. Bazhirov and M. L. Cohen, J. Phys.: Condens. Matter **25**, 105506 (2013).
[13] F. Zheng, Z. Wang, W. Kang, and P. Zhang, Sci. Rep. **3**, 2213 (2013).
[14] V. Cvetkovic and O. Vafek, Phys. Rev. B **88**, 134510 (2013).
[15] L. Fu and C. L. Kane, Phys. Rev. B **76**, 045302 (2007).
[16] H. J. Zhang, C. X. Liu, X. L. Qi, X. Dai, Z. Fang, and S. C. Zhang, Nat. Phys. **5**, 438 (2009).
[17] S. Margandonna *et al.*, Chem. Commun. (Cambridge, U. K.), 5607 (2008).
[18] M. C. Lehman, A. Llobet, K. Horigane, and D. Louca, J. Phys.: Conf. Ser. **251**, 012009 (2010).
[19] Y. Imai, Y. Sawada, F. Nabeshima, and A. Maeda, Proc. Natl. Acad. Sci. USA **112**, 1937 (2015).
[20] J. P. Hu, Phys. Rev. X **3**, 031004 (2013).
[21] J. P. Hu and N. N. Hao, Phys. Rev. X **2**, 021009 (2012).
[22] M. P. Lopez Sancho, J. M. Lopez Sancho, and J. Rubio, J. Phys. F **14**, 1205 (1984).
[23] M. P. Lopez Sancho, J. M. Lopez Sancho, and J. Rubio, J. Phys. F **15**, 851 (1985).
[24] C.-X. Liu, H. J. Zhang, B. Yan, X.-L. Qi, T. Frauenheim, X. Dai, Z. Fang, and S.-C. Zhang, Phys. Rev. B **81**, 041307(R) (2010).
[25] W. H. Zhang, Y. Sun, J. S. Zhang, F. S. Li, M. H. Guo, Y. F. Zhao, H. M. Zhang, J. P. Peng, Y. Xing, H. C. Wang, T. Fujita, A. Hirata, Z. Li, H. Ding, C. J. Tang, M. Wang, Q. Y. Wang, K. He, S. H. Ji, X. Chen *et al.*, Chin. Phys. Lett. **31**, 017401 (2014).
[26] R. Peng, X. P. Shen, X. Xie, H. C. Xu, S. Y. Tan, M. Xia, T. Zhang, H. Y. Cao, X. G. Gong, J. P. Hu, B. P. Xie, and D. L. Feng, Phys. Rev. Lett. **112**, 107001 (2014).
[27] P. Zhang, P. Richard, N. Xu, Y. M. Xu, J. Ma, T. Qian, A. V. Fedorov, J. D. Denlinger, G. D. Gu, and H. Ding, Appl. Phys. Lett. **105**, 172601 (2014).
[28] D. Huang, C.-L. Song, T. A. Webb, S. Fang, C.-Z. Chang, J. S. Moodera, E. Kaxiras, and J. E. Hoffman, Phys. Rev. Lett. **115**, 017002 (2015).

[29] J. X. Yin, Z. Wu, J. H. Wang, Z. Y. Ye, J. Gong, X. Y. Hou, L. Shan, A. Li, X. J. Liang, X. X. Wu, J. Li, C. S. Ting, Z. Wang, J. P. Hu, P. H. Hor, H. Ding, and S. H. Pan, Nat. Phys. **11**, 543 (2015).

[30] S. Kasahara, T. Watashige, T. Hanaguri, Y. Kohsaka, T. Yamashita, Y. Shimoyama, Y. Mizukami, R. Endo, H. Ikeda, K. Aoyama, T. Terashima, S. Uji, T. Wolf, H. v. Lohneysenn, T. Shibauchi, and Y. Matsuda, Proc. Natl. Acad. Sci. USA **111**, 16309 (2014).

[31] F. Yang, L. Miao, Z. F. Wang, M.-Y. Yao, F. Zhu, Y. R. Song, M.-X. Wang, J.-P. Xu, A. V. Fedorov, Z. Sun, G. B. Zhang, C. Liu, F. Liu, D. Qian, C. L. Gao, and J.-F. Jia, Phys. Rev. Lett. **109**, 016801 (2012).

[32] I. K. Drozdov, A. Alexandradinata, S. Jeon, S. Nadj-Perge, H. W. Ji, R. J. Cava, B. A. Bernevig, and A. Yazdani, Nat. Phys. **10**, 664 (2014).

[33] Z. J. Wang, P. Zhang, G. Xu, L. K. Zeng, H. Miao, X. Y. Xu, T. Qian, H. M. Weng, P. Richard, A. V. Fedorov, H. Ding, X. Dai, and Z. Fang, Phys. Rev. B **92**, 115119 (2015).

[34] G. Kresse and J. Hafner, Phys. Rev. B **47**, 558 (1993).

[35] G. Kresse and J. Furthmuller, Comput. Mater. Sci. **6**, 15 (1996).

[36] G. Kresse and J. Furthmuller, Phys. Rev. B **54**, 11169 (1996).

[37] J. P. Perdew, K. Burke, and M. Ernzerhof, Phys. Rev. Lett. **77**, 3865 (1996).

[38] H. J. Monkhorst and J. Pack, Phys. Rev. B **13**, 5188 (1976).